Pergamon

Int. J. Heat Mass Transfer. Vol. 37, No. 3, pp. 411–424, 1994

0017-9310/94 $6.00 + 0.00

Spatial and thermal features of three dimensional Rayleigh–Bénard convection

R. HERNÁNDEZ and R. L. FREDERICK
Universidad de Chile, Departamento de Ingeniería Mecánica, Casilla 2777, Santiago, Chile

(*Received* 30 *September* 1992 *and in final form* 27 *July* 1993)

Abstract—A full 3-D numerical study is reported on natural convection of air in six heated-from-below parallelepipedic enclosures. A supercritical Rayleigh number ($Ra = 8 \times 10^3$), was used in order to track the evolution of convective structures as a function of the enclosure's aspect ratio (A) only. The six situations ($1 \leqslant A \leqslant 5$) exhibit a characteristic toroidal flow pattern which can be seen, at the lowest aspect ratio, as a unicellular structure which evolves to a multicellular combination of concentric roll-cells at higher aspect ratios. The transition from one convective structure to another has the features of a flow bifurcation controlled by A. The overall Nusselt number changed continuously when the aspect ratio was increased. At the lowest aspect ratios the change was significant, but further increments in A did not produce important variations in this parameter, in the range of aspect ratios studied.

INTRODUCTION

NATURAL convection phenomena of Newtonian fluids confined in differentially heated enclosures have attracted considerable attention in recent times, because of their wide range of thermal engineering applications, such as solar energy collectors, electronic equipment cooling, solidification processes, to cite a few. From a physical point of view, natural convection in enclosures represents one of the simplest non-linear coupled flow problems providing an appropriate model to understand the role of flow instabilities and laminar flow transitions, especially in the well known heated-from-below situation (Rayleigh–Bénard convection).

This paper reports a full 3-D numerical study of the steady natural convection of a Boussinesq fluid of Prandtl number $Pr = 0.71$ (air) confined in a heated-from-below enclosure with passive vertical walls at $Ra = 8 \times 10^3$ as a finite approach to the Rayleigh–Bénard convection [1–3], in six situations characterized by their aspect ratio A.

The main task in the present work is to determine the influence of geometrical domain over the flow and heat transfer mechanisms in the heated-from-below situation. This is done through successive changes in the aspect ratio of the cavity.

In the Rayleigh–Bénard situation, convection starts when the governing parameter Ra, reaches a critical value Ra_c. Davis [2] (theoretically) and Stork and Müller [3] (experimentally) have found the marginal stability curves for different aspect ratios, finding that from $A = 1$ to $A = 5$, Ra_c decreases rapidly from $\approx 7 \times 10^3$ to $\approx 2 \times 10^3$. For infinite parallel plates, $Ra_c = 1708$ [1]. The influence of the lateral passive walls decreases as A increases. The value of $Ra = 8 \times 10^3$ therefore exceeds Ra_c for all aspect ratios we study.

The presence of the vertical walls not only affects the critical parameter, but also determines the convective structure and preferred flow pattern. As it has been shown [2–4] in longitudinal cavities, the flow pattern always consists of a finite number of roll-cells with their axes parallel to the shorter dimension of the cavity. This conclusion has also been confirmed experimentally by Symond and Peck [5] and by Yang *et al.* [6] through numerical work. These results are expected to be stable if the selected Ra is near the critical one, otherwise flow patterns degenerate to a multiplicity of time-dependent solutions which strongly depend on the initial conditions of the problem [7, 8].

The closeness of $Ra = 8 \times 10^3$ to Ra_c allows one to expect steady state solutions. As was pointed out in ref. [9], the experiments have clearly established that, beyond some value of Ra, say Ra_t, the flow becomes time-dependent. Alhers [10] has shown that Ra_t approaches Ra_c in cylindrical containers when the aspect ratio is increased. In the steady state, moreover, as Ra increases from Ra_c to Ra_t ($Ra_c < Ra < Ra_t$), a transition toward a different steady flow pattern can be expected [11]. In our situation, the dynamical governing parameter Ra is kept constant, then the aspect ratio A plays the main role as a flow pattern and heat transfer selector of steady-state solutions.

In this work the aspect ratios range from $A = 1$ to 5, because the thermal instability force δR, which is already high for $A = 5$, makes it unlikely to find steady-state solutions for $A > 5$.

To determine the overall behavior of such a complex kind of flow, we have made an extensive global and local analysis of heat transfer and flow patterns, oriented to describe and explain the evolution of convective structures, in the 3-D Rayleigh–Bénard situation, as a function of the aspect ratio A only. Cases which give steady state solutions will be studied. As it

NOMENCLATURE

A aspect ratio, l/L_x
A_c critical aspect ratio
$\mathbf{g}$ gravity vector
l length of square active walls
L_x, L_y, L_z cavity dimensions in X, Y, Z coordinates respectively
n normal dimensionless coordinate
Nu_{local} local Nusselt number
$Nu_{overall}$ overall Nusselt number
n_x, n_y, n_z number of grid points at X, Y, Z coordinates, respectively
P dimensionless pressure
Pr Prandtl number, ν/α
Ra Rayleigh number, $\mathbf{g}\beta\Delta T L_x^3/\nu\alpha$
Ra_c critical Rayleigh number at which convection starts
Ra_t critical Rayleigh number at which time-dependent solutions arise
T_h, T_c hot and cold temperatures respectively
U, V, W velocity components at X, Y, Z coordinates respectively
U_{max}, U_{min} maximum and minimum U velocity respectively
$|\mathbf{V}|_{max}$ maximum velocity projection on a given plane of velocity field
X, Y, Z dimensionless coordinates.

Greek symbols
α thermal diffusivity
β coefficient of thermal expansion
δR thermal instability force, $Ra - Ra_c$
ΔT temperature difference, $T_h - T_c$
Θ dimensionless temperature, $(T - T_c)/(T_h - T_c)$
ν kinematic viscosity.

will be seen next, the flow pattern and corresponding overall heat transfer change notoriously by only changing the relative size of the active walls. The multiple flow transitions found have the features of a flow bifurcation controlled by the aspect ratio A.

PHYSICAL AND MATHEMATICAL FORMULATION

Figure 1 shows a physical model of the heated-from-below system. A parallelepipedic enclosure with top and bottom walls at temperatures T_c and T_h respectively and insulated vertical walls is considered. The 3-D dimensionless governing equations for an incompressible Boussinesq fluid ($Pr = 0.71$) which describe the dynamics of our phenomenon are:

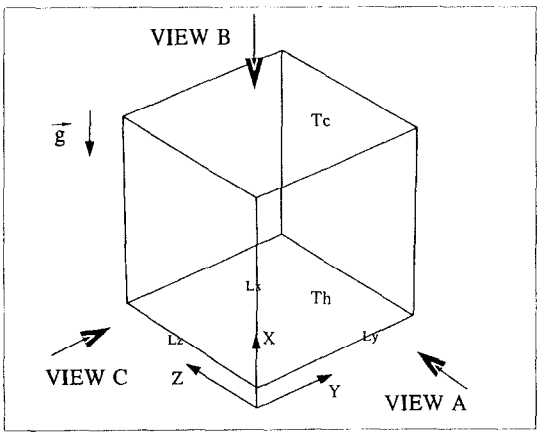

FIG. 1. Physical situation and views.

$$\frac{\partial U_i}{\partial X_i} = 0 \tag{1}$$

$$U_j \frac{\partial U_i}{\partial X_j} = -\frac{\partial P}{\partial X_i} + Ra_i Pr\Theta + Pr[\nabla^2 U_i] \tag{2}$$

$$U_i \frac{\partial \Theta}{\partial X_i} = \nabla^2 \Theta \tag{3}$$

where $Ra_x = Ra$, $Ra_y = 0$, $Ra_z = 0$ and $Ra = \mathbf{g}\beta\Delta T L_x^3/\nu\alpha$ corresponds to the Rayleigh number based on the temperature difference $T_h - T_c$ and on the distance L_x between the opposite active walls. They are expressed in tensorial form, and the velocity, pressure and temperature are scaled using as reference quantities α/L_x, $\rho(\alpha/L_x)^2$ and $(T_h - T_c)$, respectively. U_i represents each of the three dimensionless velocity components U, V, W. The boundary conditions on the cavity are; the well known no-slip condition over the walls ($U_i = 0$) and the following conditions for the temperature Θ,

$$\Theta = \begin{cases} 1 & \text{hot wall} \\ 0 & \text{cold wall} \end{cases} \tag{4}$$

with $\partial\Theta/\partial n = 0$ at the passive walls. In any of the six configurations, it was possible to define the aspect ratio $A = l/L_x$ as a characteristic geometrical parameter because we have worked only with square active walls, i.e. $l = L_y = L_z = AL_x$.

The local Nusselt number at any point in the cavity is defined by $Nu_{local} = U\Theta - \partial\Theta/\partial X$. The overall heat transfer $Nu_{overall}$ was computed by averaging the local Nusselt numbers over the active walls.

NUMERICAL METHOD

The numerical calculations were based on a primitive variable formulation of the governing equations

Table 1. Grid points used at each aspect ratio in the present numerical work

A	$n_x \times n_y \times n_z$
1	$21 \times 21 \times 21$
1.5	$21 \times 31 \times 31$
2	$16 \times 31 \times 31$
3	$16 \times 46 \times 46$
4	$15 \times 57 \times 57$
5	$13 \times 61 \times 61$

Table 2. Comparison test. Cubical side-heated cavity at $Ra = 10^3$. It was considered the midplane $Z = 0.5L_z$ for comparison

Author	Grid	U_{max}	V_{max}	$Nu_{overall}$
Fusegi	32^3	3.5013	3.5170	1.085
de Vahl Davis	21^2	3.5890	3.6290	—
Present work	21^3	3.5330	3.5328	1.084

and the discretization of the physical domain was carried out through a control volume formulation incorporating the SIMPLER algorithm of Patankar with a power law scheme which has been previously described [12]. The discrete equations were solved by an iterative tri-diagonal solver with additional criteria for fast convergence [13]. To ensure convergence, the Euclidian norm of the continuity equation residue and, at the same time, the maximum norm of the residue of the discretized energy equation, were required to fall below 10^{-3}. All dependent variables were found to reach steady state values when these conditions were met. Nusselt numbers were averaged using Simpson's rule. All calculations were carried out on an APOLLO 10000 work station. They were based on a Rayleigh number of $Ra = 8 \times 10^3$ and started with a linear temperature profile between hot and cold walls and a stagnant fluid as initial conditions. Table 1 shows the corresponding three dimensional grids used at each aspect ratio in the present work.

In order to confirm the consistency and accuracy of the computer code we made some comparisons with previous results of Fusegi *et al.* [14] for a side-heated cubical cavity ($\mathbf{g} \perp \nabla T$), and with the classical bench-mark 2-D numerical solution of de Vahl Davis [15] taking the midplane to contrast ($Z = 0.5L_z$). Good agreement was found, especially with the work of Fusegi *et al.* [14], see Table 2 for associated differences for the test solutions. An extensive grid refinement study was performed to determine the grid spacing capable to give grid-independent results. In doing so, we have solved the side-heated situation in a cubical cavity using uniform grids from 11^3 to 41^3 points. These calculations show that for the grids used in the present work (Table 1), taking the finest test grid used (41^3) as reference, the maximum associated error is 3.2% for overall Nusselt number and 2.2% for maximum and minimum velocities. The average of local Nusselt number over the hot and cold walls did not differ by more than 1.47% in any run.

Great similarity (Fig. 2) was found with an experimental work [16] in the case of a heated-from-below situation for $A = 2$ at the midplane $Z = 0.5L_z$. We took the map of isotherms as representative to check the ability of the code to represent convective structures. In addition, the three dimensional flow field for aspect ratios $A = 3, 4$ is very similar to that observed experimentally by Stork and Müller [3] at Rayleigh numbers closely above the critical one ($\sim 3 \times 10^3$). The steady-state approach adopted implies that time-dependent states are detected when they occur, by a lack of convergence of the solutions, or by oscillations of the solutions between two or more states. In our calculations ($Ra = 8 \times 10^3$), steady state solutions were not found beyond $A = 5$.

RESULTS AND DISCUSSION

Flow patterns and isograms for temperature (isotherms) are shown in Figs. 3–7 and the different views are defined as follows: views A, B, C correspond to X–Y plane along the Z axis, Z–Y plane along the X axis and Z–X plane along the Y axis, respectively. Only views of types A and B will be shown, because views C and A are identical due to symmetry of convective structures.

Flow patterns

By inspecting our velocity field maps, we can summarize the flow patterns saying that a characteristic toroidal flow formation, which evolves from an unicellular nearly toroidal pattern to a multiple concentric toroidal flow structure, controlled through systematic increments of the aspect ratio A, is observed in all cases. This basic flow structure has a vertical

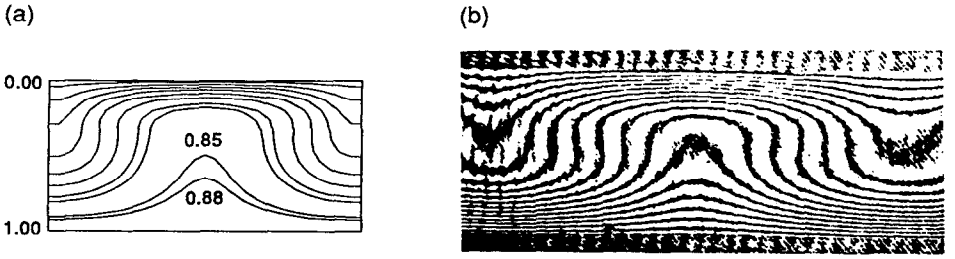

FIG. 2. Comparison between case $A = 2$ view A at $Z = 0.5L_z$ of present work (a) with experimental work of Farhadieh and Tankin (b).

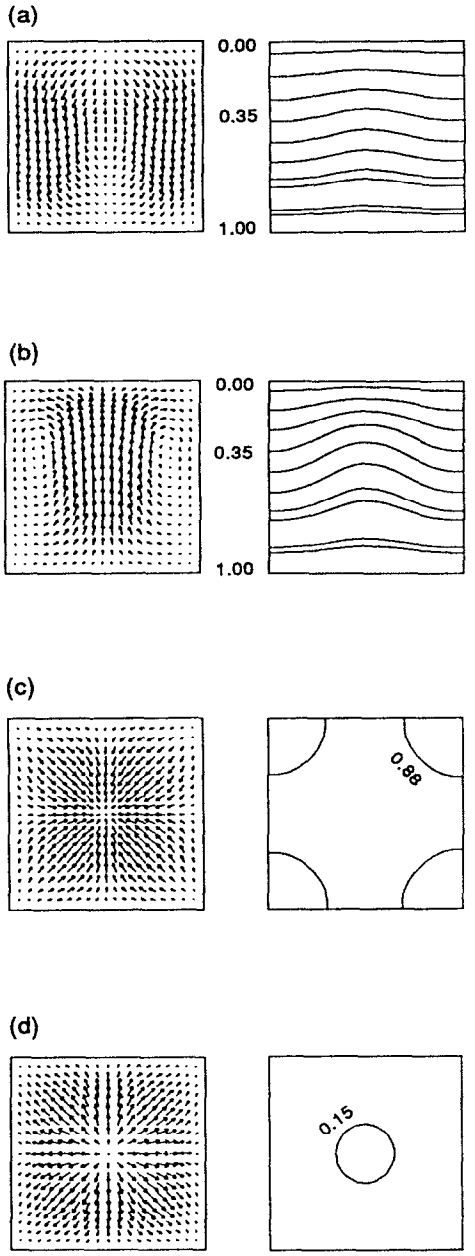

FIG. 3. Flow patterns (left) and isotherms (right) for $A = 1$. (a) View A at $Z = 0.1L_z$, $|\mathbf{V}|_{max} = 3.46$; (b) view A at $Z = 0.5L_z$, $|\mathbf{V}|_{max} = 9.09$; (c) view B at $X = 0.1L_x$, $|\mathbf{V}|_{max} = 1.84$; (d) view B at $X = 0.9L_x$, $|\mathbf{V}|_{max} = 2.85$.

symmetry axis passing through the cavity center. Because we have selected a small subset of aspect ratio values, in the present work it was not possible to predict the critical values A_c at which the flow patterns change. This idea could be the central part of a future work.

Cases $A = 1$, 1.5, 2. The three cases ($A = 1.5$ not shown) present the same dynamical behavior (Figs. 3, 4(a)–(d)). They show a single roll-cell of nearly toroidal shape, which can be explained as follows. Hot fluid, due to buoyancy forces ($Ra > Ra_c$), moves upward at the central region of the cavity, against viscous effects. When it reaches the vicinity of the top wall it turns radially towards the passive walls while it is cooled. Then it turns downward near those walls. Finally, it turns again and receives heat from the hot wall. To satisfy the mass defect produced by the lighter fluid moving at the central region, the heavier fluid is incorporated, near the bottom of the cavity, to the central ascension, closing the flow path. The case of aspect ratio $A = 2$ agreed very well with that of the work of Yang [7].

Maximum values for U velocity are found at the vertical symmetry axis of the cavity (lighter fluid ascending region) and maximum transversal velocities V, W are found at the diagonal line of Y–Z planes near the cold wall. The latter kind of path obeys a search, by the fluid, of minimum shear stress trajectories. Both the upper corners and central region offer minimum shear resistance.

Cases $A = 3$, 4. The flow pattern just described changed abruptly when the aspect ratio was varied to $A = 3$ and then to $A = 4$ (Figs. 5, 6(a)–(d)). Here two concentric toroidal roll-cells of opposite rotation sense are found to coexist. One of them fills the perimetral region of the cavity and the other one (here called internal roll-cell) is located at the central zone. The dynamics of such a complex flow, is very different from the previous cases. Here, hot fluid moves upward at the boundary between the two concentric roll-cells and downward at two regions: the central and perimetral zones of the cavity. When inspecting location for maximum U velocity values, it was found that the boundary between the perimetric and the internal roll-cell contains four fluid ascending focuses (Figs. 5, 6(d)), and in those locations hot fluid reaches their maximum U values (at $X \approx 0.5$) as in the preceding cases. On the contrary, maximum transverse V, W velocities were found in a similar region as in the preceding cases. This intricate behavior makes the most notorious difference between flow patterns of cases $A = 1$, 1.5, 2 and $A = 3$, 4.

Case $A = 5$. This aspect ratio induces an even more complex fluid pattern, as there exist three interacting concentric toroidal shape roll-cells, with alternating circulations. Hot fluid ascends at the central zone of the cavity, which belongs to the internal roll-cell, and at the roll-boundary between the perimetral and the intermediate roll-cell (Fig. 7(a)–(d)).

Cold fluid moves downward at two locations: at the vicinity of passive walls, like in all preceding cases, and at the descending roll boundary. It is very interesting to see that the general behavior of the internal roll-cell has the same appearance of cases $A = 1$, 1.5, 2, and the ascending roll boundary is similar to cases $A = 3$, 4. The local maximum of U velocity is found (Table 3) (as in cases $A = 1$, 1.5, 2), at the central zone of the cavity, and it is the highest one of all aspect

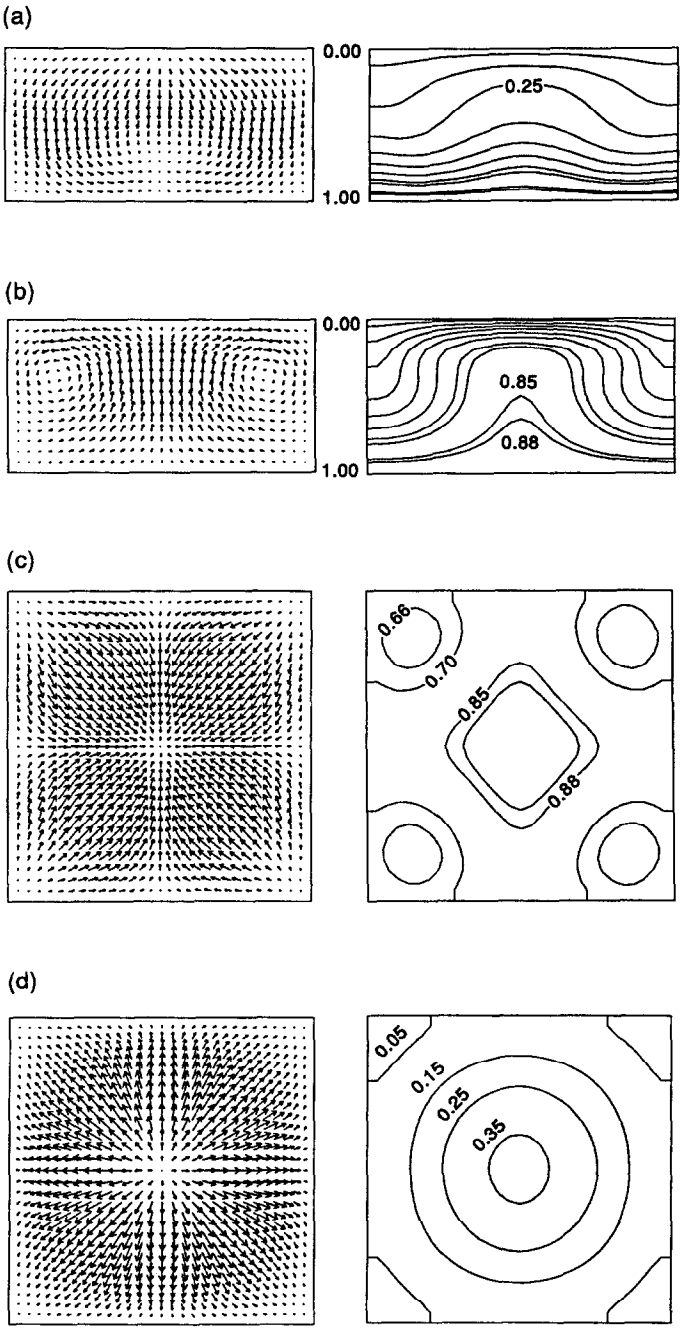

FIG. 4. Flow patterns (left) and isotherms (right) for $A = 2$. (a) View A at $Z = 1/15L_z$, $|\mathbf{V}|_{max} = 14.51$; (b) view A at $Z = 0.5L_z$, $|\mathbf{V}|_{max} = 27.52$; (c) view B at $X = 2/15L_x$, $|\mathbf{V}|_{max} = 16.53$; (d) view B at $X = 14/15L_x$, $|\mathbf{V}|_{max} = 17.82$.

ratios investigated. The local maxima for transverse V, W velocities are found at top planes near the cold wall, a region that forms part of the internal roll-cell.

Multiple flow pattern formation

The formation of convective structures can be described as follows. In the natural convection regime, the fluid inside the cavity is subject to buoyancy forces which drive the fluid upward or downward. Owing to the restriction imposed by the horizontal walls, the fluid reaching them is forced to move radially along these walls. When the fluid, in the vicinity of an active wall, has been heated or cooled to a certain extent, the positive and negative buoyancy forces begin to prevail and drive the fluid away from this wall.

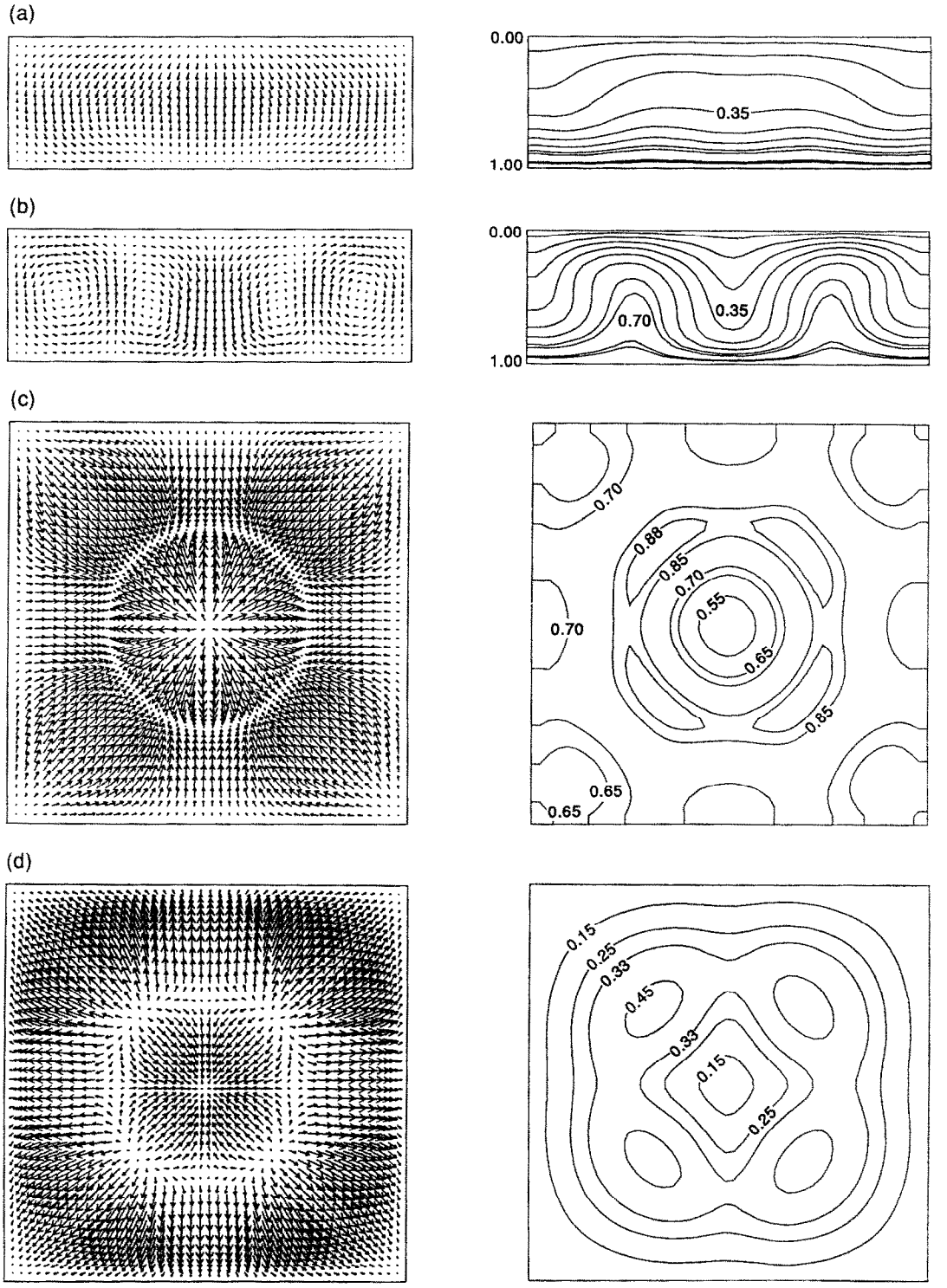

FIG. 5. Flow patterns (left) and isotherms (right) for $A = 3$. (a) View A at $Z = 2/45L_z$, $|\mathbf{V}|_{max} = 14.75$; (b) view A at $Z = 22/45L_z$, $|\mathbf{V}|_{max} = 28.98$; (c) view B at $X = 2/15L_x$, $|\mathbf{V}|_{max} = 20.26$; (d) view B at $X = 14/15L_x$, $|\mathbf{V}|_{max} = 22.54$.

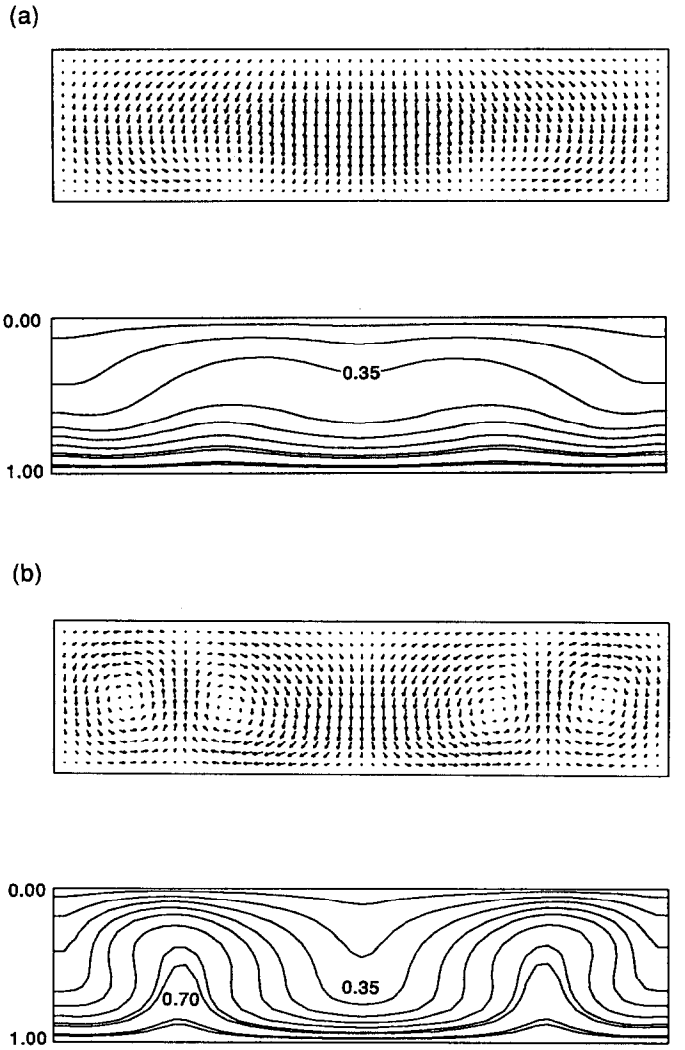

FIG. 6. Flow patterns (up) and isotherms (down) for $A = 4$. (a) View A at $Z = 1/28L_z$, $|\mathbf{V}|_{max} = 17.61$; (b) view A at $Z = 0.5L_z$, $|\mathbf{V}|_{max} = 25.96$; (c) view B at $X = 1/7L_x$, $|\mathbf{V}|_{max} = 24.86$; (d) view B at $X = 6/7L_x$, $|\mathbf{V}|_{max} = 21.83$.

New rolls are formed from the cavity center when A is increased. This can be seen noting that the flow direction near the passive walls is always downward. Table 3 and Figs. 3(b), 4(b), 5(b) and 6(b) give information for the description of the life cycle of a new roll. A new roll starts with the establishment of a centrally ascending or descending flow, which turns radially outward when it reaches a horizontal wall.

Table 3. Maximum and minimum vertical velocities vs aspect ratio

A	U_{max}	U_{min}
1	9.682	−4.168
1.5	28.461	−15.818
2	28.819	−16.958
3	22.794	−31.219
4	25.455	−24.701
5	30.609	−27.033

When a roll is formed, the absolute value of velocity at the vertical axis (upward or downward) first increases with A, then it passes through a maximum and finally decreases at the end of the cycle. The initial increase is associated with the decrease of Ra_c with A, which allows higher velocities to be obtained at higher A owing to the reduced shear effect of the passive walls. The later decrease in the absolute value of central vertical velocity is caused by an expansion of the cross section for central flow caused by the increase in A. (By comparing Figs. 5(b) and 6(b) we see that at $A = 3$, roughly 32% of the cross section is occupied by descending flow. The corresponding percentage at $A = 4$ is 43%.) The cycle of a roll ends with the formation of a new roll. In this condition, the fluid flowing upward or downward at the center will not necessarily turn radially outward when it reaches the upper or lower wall, respectively. Outward turning begins to be associated with a longer radial trajectory,

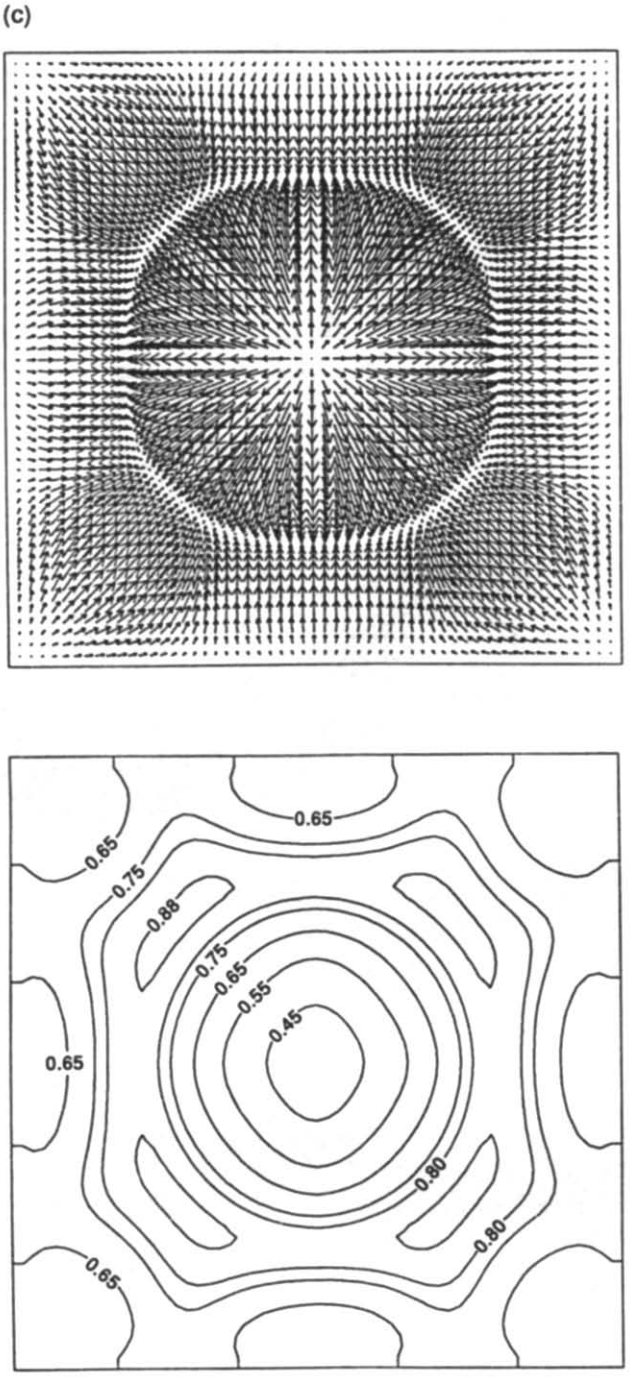

FIG. 6.—*Continued.*

so a part of the fluid looks for a shorter path along the active wall and turns inward. This is the beginning of the formation of a new roll.

The velocity changes involved in this process are very significant for the first two rolls. For the third one, when Ra_c is very similar to Ra, the vertical velocity cannot have very important increases. A fourth roll has not been detected, because the flow structure appears to be time-dependent for $A > 5$.

The mechanism of roll formation suggests the existence of characteristic radial distances identifying the roll-boundaries, related with the critical aspect ratios at which the flow patterns change.

Heat transfer

Both the three dimensional flow field and the corresponding heat transfer rate change significantly when the aspect ratio is increased, so that, the overall

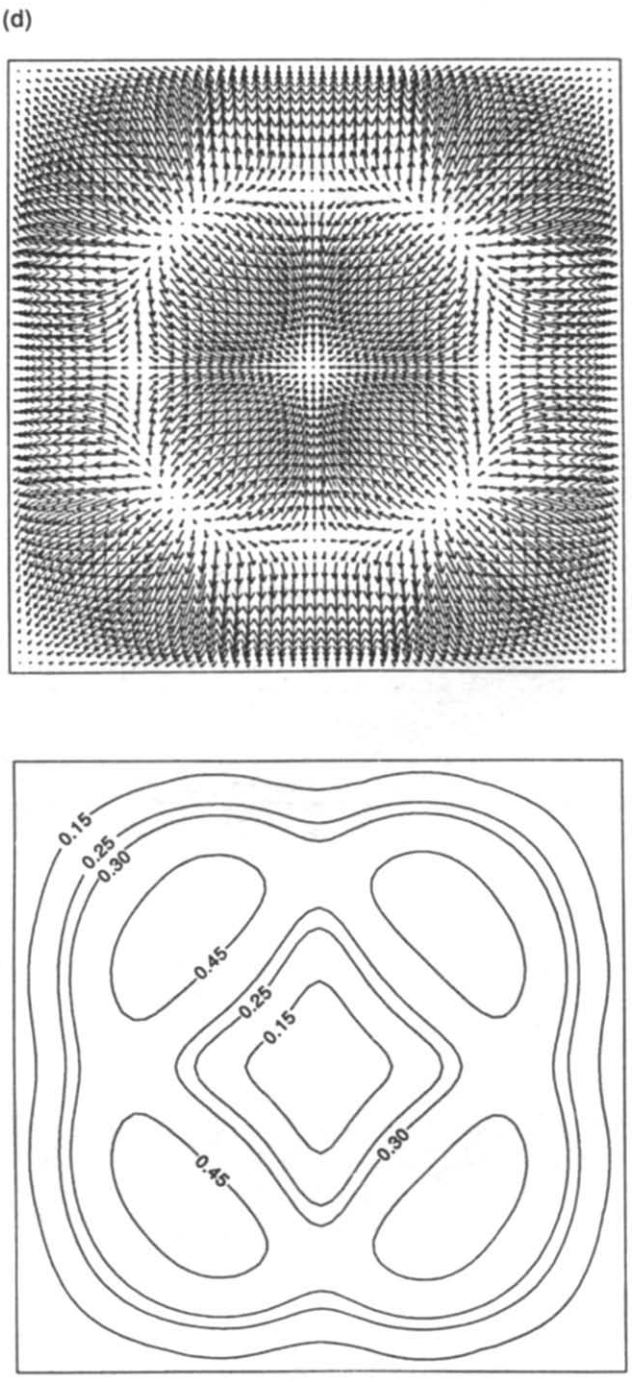

FIG. 6.—*Continued.*

Nusselt number grows rapidly at first, then it grows at a much slower rate as the number of roll-cells increases.

Figures 8(a)–(f) show the local Nusselt number Nu_{local} distribution at the central X–Y plane ($Z = 0.5L_z$). The groups of curves shown on each graph correspond to several values of X coordinate. From all graphs we can easily distinguish the essential role of lighter fluid ascending regions, where local maximum values of Nu_{local} occur. This parameter reaches local maximum values at $X = 0.5$ in all tested cavities, located at roll boundaries in cases $A = 3$, 4 and at the central region in cases $A = 1$, 1.5, 2, 5. The number of local maximum and minimum values of Nu_{local} depends exclusively on the number of interacting roll-cells. Cases $A = 1$, 1.5, 2 show only one maximum value at the central zone because of the central ascension of hot fluid (Figs. 8(a)–(c)). Cases

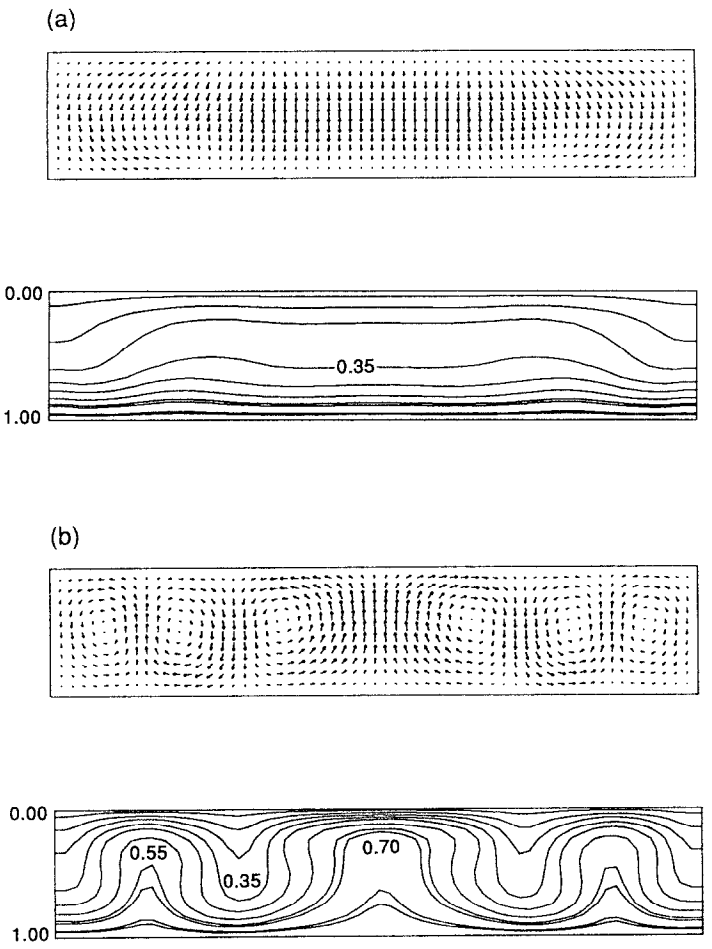

FIG. 7. Flow patterns (up) and isotherms (down) for $A = 5$. (a) View A at $Z = 1/30L_z$, $|\mathbf{V}|_{max} = 18.19$; (b) view A at $Z = 0.5L_z$, $|\mathbf{V}|_{max} = 30.45$; (c) view B at $X = 1/6L_x$, $|\mathbf{V}|_{max} = 21.16$; (d) view B at $X = 5/6L_x$, $|\mathbf{V}|_{max} = 24.02$.

$A = 3$, 4 exhibit two maximum values, which are found at the ascending roll boundary (Figs. 8(d), (e)), and case $A = 5$ shows three local maximum values. One of them is due to lighter fluid ascension at the central zone of the cavity, and the others are related to the lighter fluid which moves upward at a roll boundary (Fig. 8(f)). The minimum values of Nu_{local} are caused, in all the situations, by the downward movement of heavier fluid.

Figure 9 shows the overall Nusselt number as a function of A. At low values of A, $Nu_{overall}$ grows rapidly with the aspect ratio, tending to become more uniform at higher aspect ratios.

The shape of the curve can be explained as follows: at any given aspect ratio, the value of critical Rayleigh number results from the balance between buoyancy forces and flow restrictions. At $A = 1$, our $Ra = 8 \times 10^3$ exceeds the critical Rayleigh number only slightly, and therefore low velocity levels are found. As A grows to values of 1.5 and 2, Ra_c significantly departs from Ra and, as a consequence, the vertical velocity levels are greatly increased (see Table 3), leading to a rapid increase in heat transfer. As already explained [3], Ra_c does not vary significantly with A for $A > 2$, so the velocity levels (Table 3) and overall Nusselt number (Fig. 9) are seen to vary at a slower rate.

When the aspect ratio is increased with the number of roll cells kept constant (as happens at aspect ratios from 1 to 2), $Nu_{overall}$ grows. This is associated with the already described mechanism of roll formation. Initially, the increase in vertical velocity determines a growth in $Nu_{overall}$. Later, the increase in the flow area available for upward/downward flow, produces the same effect.

As A grows from 2 to 3, the flow pattern undergoes a transition from one to two roll cells. This is accompanied by a momentary decrease in $Nu_{overall}$, associated to the change from a centrally ascending flow structure to a centrally descending one, with a high downward central velocity. The progressive reductions in this velocity allow an increase in $Nu_{overall}$ as A is increased. On the contrary, the transition from $A = 4$ to 5 (2 to 3 roll cells), is accompanied by a

(c)

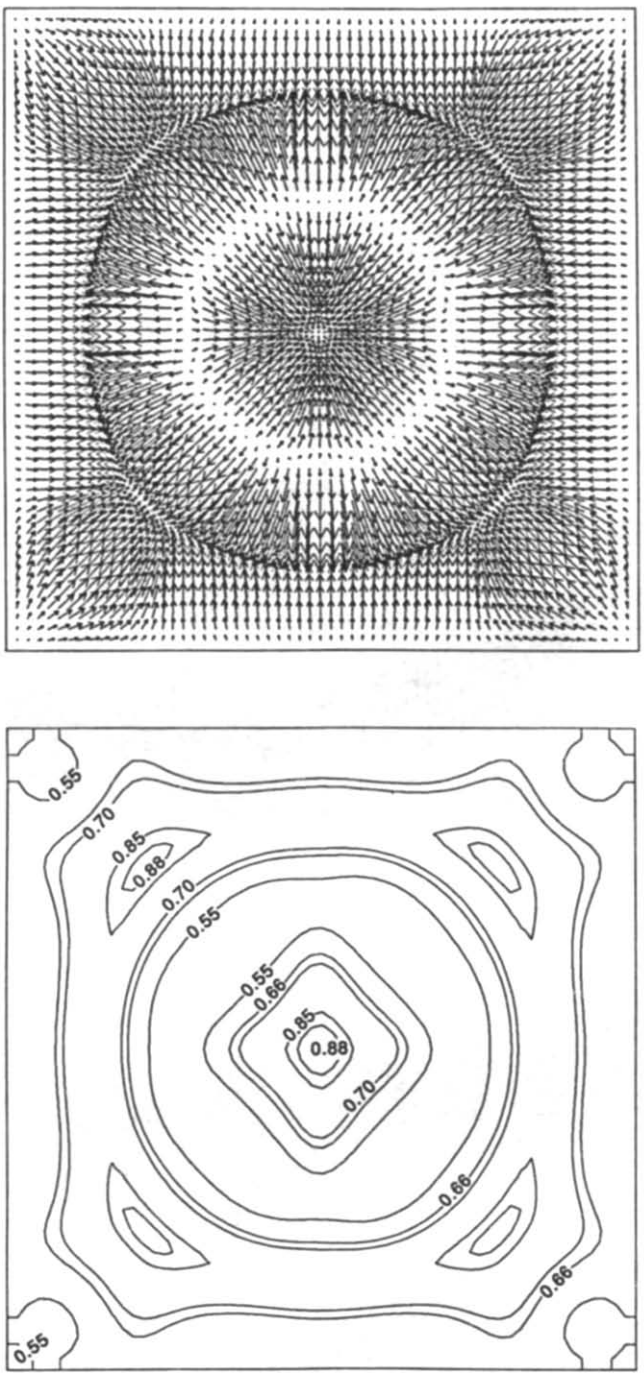

FIG. 7.—*Continued.*

slight heat transfer increase. This is associated with the reestablishment of vertical upward flow at the cavity center.

CONCLUDING REMARKS

A detailed numerical study was performed on 3-D Rayleigh–Bénard convection at $Ra = 8 \times 10^3$. The most evident result of these calculations is the flow pattern and heat transfer dependence on the cavity aspect ratio. We found a nearly toroidal flow structure which evolves from an unicellular to a multicellular flow pattern, consisting of concentric roll-cells, when the aspect ratio was systematically increased from $A = 1$ to 5. For $A = 1, 1.5, 2$ the flow pattern consists of a single, nearly toroidal roll-cell. When $A = 3, 4$ we

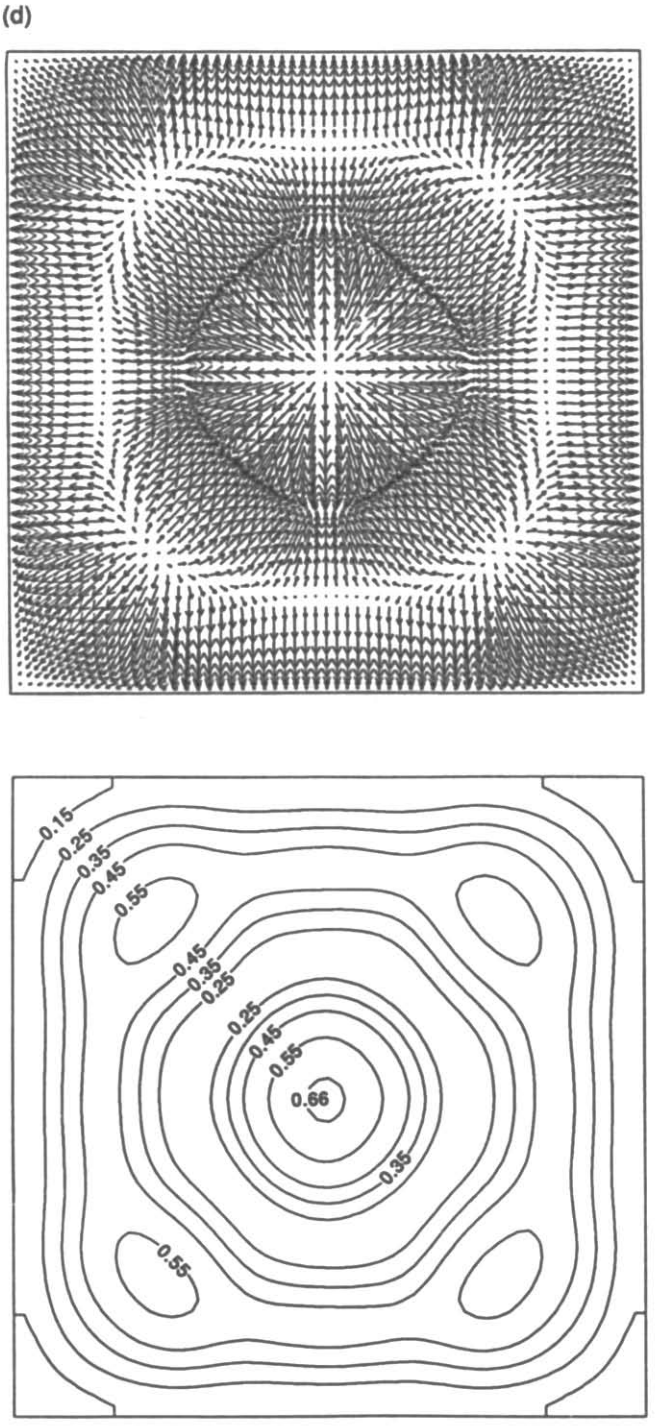

FIG. 7.—*Continued.*

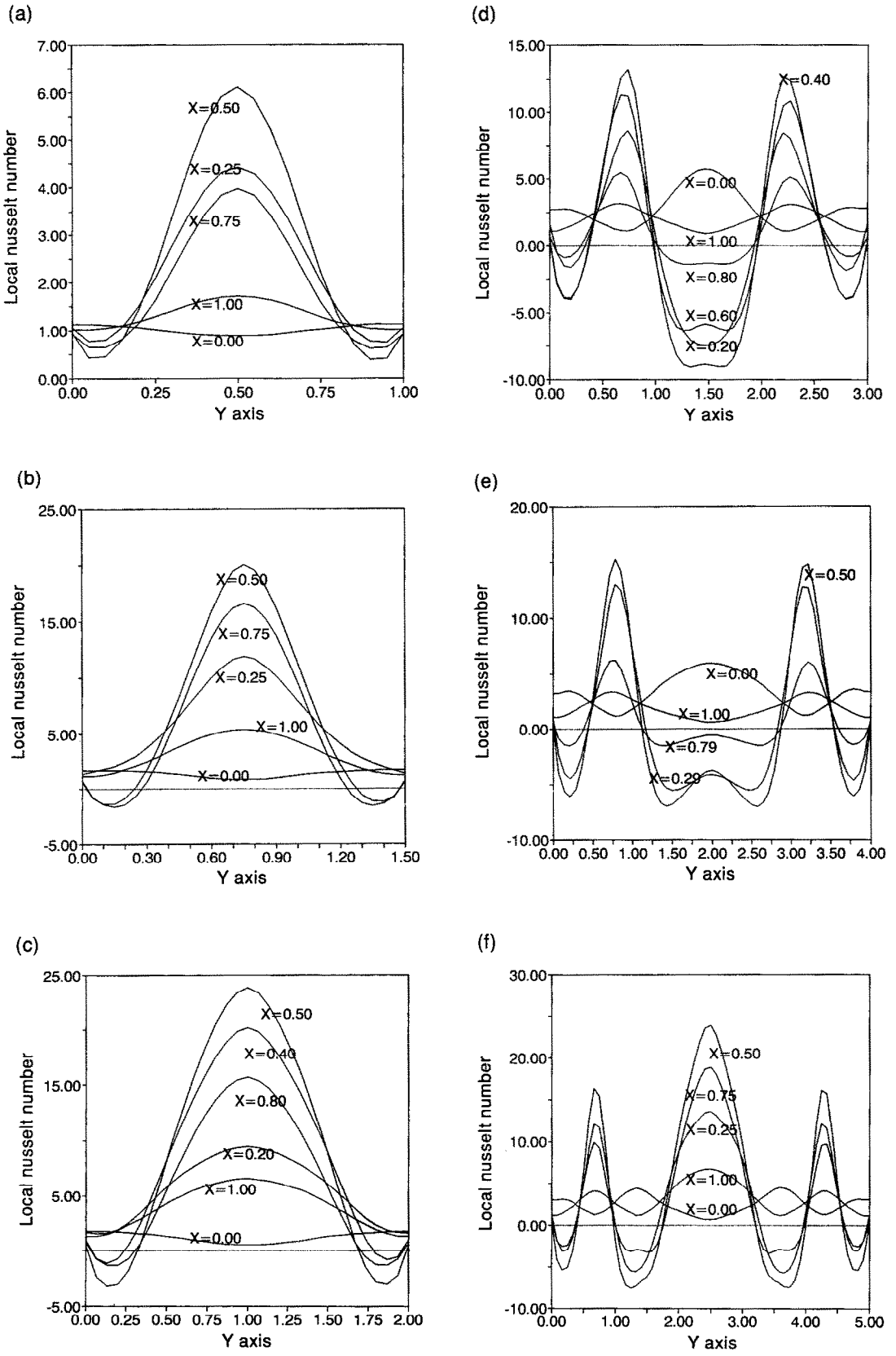

FIG. 8. Local Nusselt number distribution for midplane X–Y at $Z = 0.5L_z$. (a) $A = 1$, (b) $A = 1.5$, (c) $A = 2$, (d) $A = 3$, (e) $A = 4$, (f) $A = 5$.

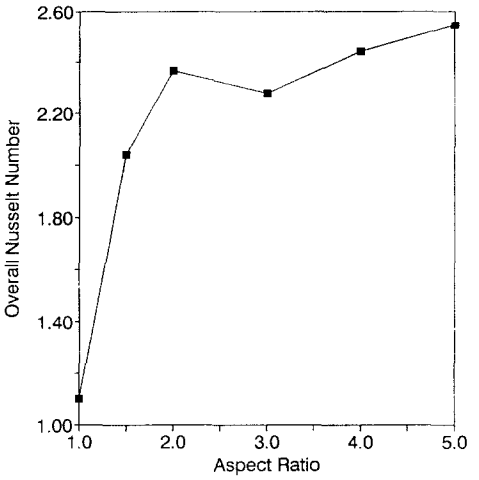

FIG. 9. Evolution of overall Nusselt number with aspect ratio.

observed two interacting concentric roll-cells. Finally, when $A = 5$, coexistence of three interacting roll-cells with alternating circulations was found. The mechanism of formation of successive rolls was described. Only cases which give steady-state flow structures were reported. Heat transfer also changes when A is varied. The overall Nusselt number increases by a factor of almost two at first (from $A = 1$ to 2) then it tends to become more uniform as the number of roll-cells increases. The flow transition from one overall convective pattern to another has the features of a bifurcation, which takes place at certain critical aspect ratio A_c. It will be of great interest, in a future work, to find the critical aspect ratios associated to this kind of bifurcation.

REFERENCES

1. S. Chandrasekhar, *Hydrodynamic and Hydromagnetic Stability*, Chap. 2. Dover, New York (1981).
2. S. H. Davis, Convection in a box: linear theory, *J. Fluid Mech.* **30** (3), 465–478 (1967).
3. K. Stork and U. Müller, Convection in boxes: experiments, *J. Fluid Mech.* **54** (4), 599–611 (1972).
4. M. P. Arroyo and J. M. Savirón, Rayleigh–Bénard convection in a small box: spatial features and thermal dependence of the velocity field, *J. Fluid Mech.* **235**, 325–348 (1991).
5. J. G. Symons and M. K. Peck, Natural convection heat transfer through inclined longitudinal slots, *J. Heat Transfer* **106**, 824–829 (1984).
6. H. Q. Yang, K. T. Yang and J. R. Lloyd, Laminar natural convection flow transitions in tilted three-dimensional longitudinal rectangular enclosures, *Int. J. Heat Mass Transfer* **30**, 1637–1644 (1987).
7. H. Q. Yang, K. T. Yang and J. R. Lloyd, Three-dimensional bimodal buoyant flow transitions in tilted enclosures, *Int. J. Heat Fluid Flow* **9**, 90–97 (1988).
8. P. Bergé, Y. Pomeau and C. Vidal, *Order within Chaos. Towards a Deterministic Approach to Turbulence*, Chap. 5. Wiley, New York (1984).
9. C. Normand, Y. Pomeau and M. G. Velarde, Convective instability: A physicist's approach, *Rev. Modern Phys.* **49**, 581–624 (1977).
10. G. Alhers and R. P. Behringer, Evolution of turbulence from the Rayleigh–Bénard instability, *Phys. Rev. Lett.* **40**, 712–716 (1978).
11. D. S. Riley and K. H. Winters, A numerical bifurcation study of natural convection in tilted two-dimensional porous cavity, *J. Fluid Mech.* **215**, 309–329 (1990).
12. R. Hernández, Modelación numérica tridimensional del fenómeno de convección natural en cavidades de razón de aspecto variable, Master Thesis, Universidad de Chile, Santiago, Chile (1992).
13. J. P. Van Doormaal and G. D. Raithby, Enhancements of the simple method for predicting incompressible fluid flows, *Numer. Heat Transfer* **7**, 147–163 (1984).
14. T. Fusegi, J. M. Hyun, K. Kuwahara and B. Farouk, A numerical study of three-dimensional natural convection in differentially heated cubical enclosure, *Int. J. Heat Mass Transfer* **34**, 1543–1557 (1991).
15. G. de Vahl Davis, Natural convection of air in a square cavity: a bench mark numerical solution, *Int. J. Numer. Meths. Fluids* **3**, 249–264 (1983).
16. R. Farhadieh and R. S. Tankin, Interferometric study of two-dimensional Bénard cells, *J. Fluid Mech.* **66** (4), 739–752 (1974).